Sensitivity study of the generation of mesoscale eddies in a numerical model of Hawaii islands

M. Kersalé[1], A. M. Doglioli[1], and A. A. Petrenko[1]

[1]Aix-Marseille Université; CNRS; IRD; LOPB-UMR 6535, Laboratoire d'Océanographie Physique et Biogéochimique, OSU/Centre d'Océanologie de Marseille, France.

Abstract. The oceanic circulation around the Hawaiian archipelago is characterized by a complex circulation and the presence of mesoscale eddies west of the islands. These eddies typically develop and persist for weeks to several months in the area during persistent trade wind conditions. A series of numerical simulations on the Hawaiian region has been done in order to examine the relative importance of wind, inflow current and topographic forcing on the general circulation and the generation of eddies. Moreover, numerical cyclonic eddies are compared with the one observed during the cruise E-FLUX (Dickey et al., 2008). Our study demonstrates the need for all three forcings (wind, inflow current and topography) to reproduce the known oceanic circulation. In particular, the cumulative effect plays a key role on the generation of mesoscale eddies. The wind-stress-curl, via the Ekman pumping mechanism, has also been identified as an important mechanism upon the strength of the upwelling in the lee of the Big Island of Hawaii. In order to find the best setup of a regional ocean model, we compare more precisely numerical results obtained using two different wind databases : COADS and QuikSCAT. The main features of the ocean circulation in the area are well reproduced by our model forced by both COADS and QuickSCAT climatologies. Nevertheless, significant differences appear in the levels of kinetic energy and vorticity. The wind-forcing spatial resolution clearly affects the way in which the wind momentum feeds the mesoscale phenomena. The higher the resolution, the more realistic the ocean circulation. In particular, the simulation forced by QuikSCAT wind data reproduces well the observed energetic mesoscale structures and their hydrological characteristics and behaviors.

Correspondence to: M. Kersalé
marion.kersale@univmed.fr

1 Introduction

The oceanic area around the Hawaiian archipelago exhibits a complex circulation characterized by the presence of mesoscale eddies west of the islands. This circulation is mainly due to the effects of the archipelago topographic forcing on both the North Equatorial Current (NEC) and the trade wind. Indeed, the blocking effect of the Hawaiian islands bathymetry on the oceanic flow is similar to the one of these islands' topography on the wind.

The NEC is a broad westward flow, constituting the southern part of the North Pacific subtropical gyre. When the NEC encounters the island of Hawaii, it is deflected towards the south, but also generates a northern branch (Lumpkin, 1998). The northern branch is known as the North Hawaiian Ridge Current (NHRC), flowing coherently along the islands at an average speed of 0.10 - 0.15 ms^{-1} (Qiu et al., 1997). The wake generated by the Hawaiian island is thought responsible for the formation of the Hawaiian Lee Counter Current (HLCC).

By a classical mechanism of formation of eddies in the lee of an obstacle, the wake can also generate mesoscale eddies, as indicated by the observations reported downstream of Gran Canaria Island (Aristegui et al., 1994, 1997; Barton et al., 2000). In the case of Hawaii, south (north) of the HLCC these eddies are typically anticyclonic (cyclonic) (Lumpkin, 1998).

A second mechanism could also explain the formation of an important counter-current (here the HLCC) and mesoscale eddies (whether in Hawaii or Gran Canaria). Lumpkin (1998) showed that there is an eddy-to-mean kinetic energy conversion at the latitude of the HLCC immediately west of the Island of Hawaii. By a simple Sverdrup balance, Chavanne et al. (2002) predict an HLCC from the wind stress curl dipole in the lee of the island of Hawaii. As explained by Smith and Grubisic (1993), the Hawaiian archipelago presents a series of high vertical obstacles to the wind. The

islands act as barriers to the trade winds, which are confined below the tropopause and constrained to flow around the topography (Chavanne et al., 2002). The wind stress variations in the lee of the Hawaiian Islands drive divergent and convergent Ekman transports in the upper layer of the ocean. And, in particular, the acceleration of the persistent northeasterly trade winds through the Alenuihaha Channel separating these islands is the second mechanism generating mesoscale eddies (Patzert, 1969). **West of the islands, this mechanism can create cyclonic eddies south of** $20°$**N and anticyclonic eddies north of** $20°$**N.**

Historical hydrographic and satellite data sets (Patzert, 1969; Lumpkin, 1998; Chavanne et al., 2002; Seki et al., 2001, 2002; Bidigare et al., 2003) indicate that mesoscale eddies typically develop and persist for weeks to several months west of the Hawaiian archipelago during persistent trade wind conditions. Moreover, interdisciplinary observations of mesoscale eddies were recently made west of the Big Island of Hawaii, combining different data from ships, surface drifters and satellite sensors (Dickey et al., 2008, project E-FLUX). During the cruises E-Flux I and III, two cold-core cyclonic mesoscale eddies, *Noah* and *Opal*, respectively, have been found.

To simulate the oceanic circulation around the Hawaiian islands, we used a version of the model ROMS (Regional Oceanic Modeling System) provided with the following ROMSTOOLS [http://roms.mpl.ird.fr]. This modeling system is increasingly used, since its functionality and robustness have been demonstrated. Different physical constraints can be implemented with regard to boundary conditions and bottom stress. Different databases can also be used to provide atmospheric forcing to ROMS model, such as COADS (Comprehensive Ocean-Atmosphere Data Set Project) and data collected by NASA's SeaWinds Scatterometer aboard QuikSCAT.

Dong and McWilliams (2007) used the model ROMS to study vortex shedding by deep water islands and topographic eddy forcing in the Southern California Bight. Yoshida et al. (2010) studied the wind forcing of Hawaiian eddies. They found that, in the immediate lee southwest of Hawaii (18.9°N-20°N, 158°W-156.7°W), eddy signals have a predominant 60-day period and a short life-span. They noticed that the observed eddies originate in the southwest corner of Hawaii and are induced by the local wind stress curl variability associated with the blocking of the trade wind by the island of Hawaii. Jiménez et al. (2008) performed several experiments to study the relative importance of topographic and wind forcing on oceanic eddy shedding by an isolated, tall, deep water island. They applied the model to the case of eddies shed by the island of Gran Canaria. They found that wind forcing alone is not sufficient to force an oceanic Von Karman vortex street in the lee of the island and that topographic forcing is necessary. In their case, the wind forcing is not the main mechanism responsible for oceanic vortex shedding, it acts as a trigger mechanism when the incident

current alone is not sufficiently energetic to produce vortex shedding.

As regards wind forcing, monthly mean values from COADS were compared to monthly mean wind speed and direction from Canadian weather buoys in the northeast Pacific (Cherniawsky and Crawford, 1996). Wind speed measurements from QuikSCAT scatterometer were validated by comparison with independent data. For instance, they were compared with meteorological analyses (Renfrew et al., 2009) over the Denmark Strait, or with wind speeds computed from RADARSAT-1 synthetic aperture radar (SAR) in the Gulf of Alaska (Monaldo et al., 2004). Concerning ocean modeling, the influence of COADS versus QuickSCAT wind data on oceanic circulation was analyzed in the California Current System (Penven et al., 2002). Calil et al. (2008) have done numerical modeling simulations of the ocean response to realistic wind forcing in the lee of the Hawaiian Island chain. Since we use the same methodology, we stress, in this paper, the similarities and differences between their and our results. On the North equatorial central Pacific, an ocean model forced by COADS wind versus one forced by the NCEP-NCAR (National Centers for Environmental Prediction - National Center for Atmospheric Research) reanalysis wind were used to compare the observations of ocean heat content (Wu and Xie, 2003). Independent observations of oceanic circulation were investigated with an ocean model forced by QuikSCAT wind data in different regions: the Pacific system (Xie et al., 2001) and the Southern Benguela upwelling system (Blanke et al., 2005).

The main purpose of this study is to analyze the relative importance of topography and wind forcing on the Hawaiian oceanic circulation and eddies generation, with particular attention to wind-driven mesoscale eddy generation simulated with both COADS and QuikSCAT wind data.

The paper is organized as follows: section 2 introduces briefly the numerical model, the main simulation and eddy tracking parameters. Section 3 presents the model sensitivity and a discussion about the variability in the surface wind stress. This part will allow us to analyze whether the model reproduces the generation of mesoscale eddies west of the Hawaiian archipelago. In section 4, we analyze which simulation is the more realistic and whether one forcing is predominant. Our conclusions are drawn in section 6.

2   Materials and Methods

2.1   Ocean Model

Our circulation model is based on the IRD (Institut de Recherche pour le Développement) version of the Regional Ocean Modeling System (ROMS). The reader is referred to Shchepetkin and McWilliams (2003, 2005) for a more complete description of the numerical code. The model domain

extends from 154°W to 161°W and from 18°N to 23°N (Fig. 1).

figure

Its grid, forcing, initial and boundary conditions were built with the ROMSTOOLS package (Penven et al., 2010). The model grid is 69×53 points with a resolution of $\frac{1}{10}^\circ$ corresponding to about 10 km in mean grid spacing, which allows a correct sampling of the first baroclinic Rossby radius of deformation throughout the whole area (about 60 km according to Chelton et al., 1998). The horizontal grid is isotropic with no introduction of asymmetry in the horizontal dissipation of turbulence. It therefore provides a fair representation of mesoscale dynamics. The model has 32 vertical levels, and the vertical s-coordinate is stretched for boundary layer resolution. The bottom topography is derived from a $2'$ resolution database (Smith and Sandwell, 1997). Although a numerical scheme associated with a specific equation of state limits errors in the computation of the horizontal pressure gradient (Shchepetkin and McWilliams, 2003), the bathymetry field, h, must be filtered to keep the slope parameter, r, as $r = \frac{|\nabla h|}{2h} \leq 0.25$ (Beckmann and Haidvogel, 1993). Respecting the CFL criterion, the external (internal) timestep has been fixed equal to 12s (720s).

At the four lateral boundaries facing the open ocean, the model solution is connected to the surroundings by an active, implicit and upstream-biased radiation condition (Marchesiello et al., 2001). Under inflow conditions, the solution at the boundary is nudged toward temperature-, salinity- and geostrophic velocity-fields calculated from Levitus 1998 climatology (NODCWOA98 data provided by the NOAA/OAR/ESRL PSD, Boulder, Colorado, USA, from their Web site at http://www.cdc.noaa.gov/), which is also used for the initial state of the model. The nudging timescale for inflow and outflow (τ_{in}, τ_{out}) are set to (1 day, 1 year) for the tracer fields and (10 days, 1 year) for the momentum fields. The geostrophic velocity (U_{geo}) is referenced to the 2000 m level. The width of the nudging border is 100 km, and the maximum viscosity value for the sponge layer is set to 800 m^{2}s^{-1}.

Bottom boundary conditions for momentum are computed by assuming a logarithmic velocity profile and using a bottom roughness ($Z_{ob} = 1.10^{-2}$m) to determine a quadratic drag coefficient for a typical stress boundary condition of $\overrightarrow{\tau_b} = C_d \rho_o \overrightarrow{u} |\overrightarrow{u}|$ where τ_b is the bottom frictional stress, ρ_0 the water density, C_d the drag coefficient and $\overrightarrow{u}$ the bottom current. The drag coefficient is defined as $C_d = \frac{k}{ln(z/Z_{ob})}$ ranging from a minimum of 10^{-4} and a maximum of 10^{-1} coefficient with k the Von Karman constant.

At the surface, the heat and fresh water fluxes introduced in the model are extracted from the Comprehensive Ocean-Atmosphere Data Set (COADS, Da Silva et al., 1994). As regards wind stress, two different databases are used in this work : (i) a monthly mean climatology computed from COADS dataset (1945-1989) giving data with spatial resolution of $\frac{1}{2}^\circ$; (ii) a monthly mean climatology computed from satellite-based QuikSCAT dataset (2000-2007, Callahan and Lungu, 2006) gridded at $\frac{1}{4}^\circ$ resolution.

Table 1 summarizes the performed numerical experiments. In all cases, we run 10-year simulations with model outputs averaged and stored every 3 days of simulation.

Name	Wind forcing	Advection	Drag Coeff.
Run-A	none	U_{geo}	C_d
Run-B	none	$2U_{geo}$	C_d
Run-C	QuikSCAT	none	C_d
Run-D	QuikSCAT	U_{geo}	none
Run-E	COADS	U_{geo}	C_d
Run-F	QuikSCAT	U_{geo}	C_d

Table 1. Summary of the performed numerical experiments, the relatives names and the forcings

The two first experiments (Run-A and Run-B) are made with no wind forcing and different values for the inflow velocities at the open boundary. In the third experiment (Run-C), the inflow velocity is set to zero and the wind forcing comes from the QuikSCAT database. In Run-D, the drag coefficient is set equal to zero. The two last experiments, with both advection and bottom friction, allow to compare the effect of different wind forcing dataset : COADS (Run-E) and QuikSCAT (Run-F).

2.2 Eddy tracking and characterization

To detect eddies, we select a threshold value of the sea surface height (ssh) of |5| cm. We choose to set this value to one third of the typical ssh anomaly generated by anticyclonic eddies in the Hawaii region (i.e. 15 cm, according to Firing and Merrifield, 2004). Each cyclone (anticyclone) is then listed by the letter $C(A)$ followed by the number corresponding to their temporal appearance. To indicate in which experiment eddies are observed, a letter listing the Run is added at the end of each name of the eddy.

In the following we focus on numerical cyclones chosen because they are spatially and temporally representative of cyclone *Opal* studied during the cruise E-FLUX III (March 10-28, 2005) and observed on SST satellite images from February to April of that year (Nencioli et al., 2008). **The characteristics used to chose numerical cyclones resembling the most *Opal* are the following : generation date, position and life-time. We propose a quantitative comparison between the numerical eddies and *Opal* based on eddy characteristics' statistics during the last five years of simulation. Moreover we illustrated this comparison with figures issued from the tenth year of simulation.**

Following Dickey et al. (2008), we define the radial extent of the eddy as the distance between the locations where isopycnal and isotherm surfaces become nearly horizontal. Indeed, according to these authors, the $\sigma_{t_{24}}$ (i.e. $\sigma_t =$

$24\,\mathrm{kgm^{-3}}$) isopycnal surface proved to be an important reference in determining the general characteristics of cyclones in this area. Moreover, we calculate the east-west (north-south) components of the horizontal velocity vector along a north-south (east-west) transect for the most realistic numerical eddy. In this way we can both (i) estimate the position of the eddy center, as the location where the components of the horizontal velocity are very small and (ii) calculate the eddy radius, as the maximum distance until which, starting at the center, the intensity of the barotropic velocity increases linearly (corresponding to the solid body rotation, e.g. Nencioli et al., 2008). This latter distance allows us to also check the previous evaluation of the eddy extent.

3　Results

3.1　Kinetic energy

The temporal evolutions of the volume-averaged kinetic energy for all simulations are reported in Fig. 2. The Run-A results are characterized by the lowest kinetic energy and smallest temporal variability. When the speed of the currents at the boundary is more intense (Run-B), the 10-year mean value of volume-averaged kinetic energy goes from 22 to 27 $\mathrm{cm^2 s^{-2}}$. This mean value is of the same order than the one of the Run-C result (28 $\mathrm{cm^2 s^{-2}}$) but the temporal variability of Run-C is higher than the one of Run-B. The Run-D results are characterized by the highest kinetic energy (32 $\mathrm{cm^2 s^{-2}}$) and largest temporal variability. The Run-F results are generally more energetic (30 $\mathrm{cm^2 s^{-2}}$) than the Run-E ones (27 $\mathrm{cm^2 s^{-2}}$). Moreover, the kinetic energy has a lower temporal variability in Run-E than in Run-F. We can classify these simulations, from the less to the more energetic with reference to the 10-year mean value of volume-averaged kinetic energy : Run-A (22 $\mathrm{cm^2 s^{-2}}$) < Run-B = Run-E (27 $\mathrm{cm^2 s^{-2}}$) < Run-C (28 $\mathrm{cm^2 s^{-2}}$) < Run-F (30 $\mathrm{cm^2 s^{-2}}$) < Run-D (32 $\mathrm{cm^2 s^{-2}}$). figure

figure

3.2　Topographic forcing with advection and no wind

In this experiment, the objective is to analyze the importance of the topographic forcing on the Hawaiian oceanic circulation. With this aim in view, wind forcing is suppressed and the intensity of the inflow velocity is set to U_{geo} in Run-A and has been doubled ($2U_{geo}$) in Run-B. **In general, the annually averaged circulation of Run-A does not reproduce the NEC and the HLCC (Fig. 3-a). In the Run-B (Fig. 3-b) the NEC split is well reproduced. To study the mesoscale structures, the situation on August 22 is presented in both Run-A and Run-B (Fig. 4).** Mesoscale structures dominate the flow field with cyclonic and anticyclonic eddies present in the two simulations. The vortex shedding leads to the formation of a street of successive cyclonic and anticyclonic eddies, looking like a Karman vortex street, downstream the Big Island. The numerical results show that the formation of cyclonic eddies frequently occurs on the lee side of other islands, as indicated by the observations reported downstream of Lanai Island (Dong et al., 2009). In Run-A, anticyclones tend to dominate south of $19-20°$N and cyclones to be more present in the north. In Run-B, a current is accelerated through the Alenuihaha Channel, inducing vorticity (Fig. 4-b). This is not observed in Run-A. This contribution of vorticity induces the formation of anticyclonic eddies between two cyclones regions. If we compare the two simulations, the structures from Run-B are more coherent and intense than the ones from Run-A. In Run-B, the vortex shedding frequency increases in time with increasing velocity current. We can calculate the Strouhal number $S_t = D/TU$ defining the eddy shedding frequency, where D is the diameter of the Big Island (100 km), T the shedding period and U the current speed. The period for eddy shedding is roughly 60 days (30 days) for Run-A (Run-B). The mean value of the current speed at 10-m depth is equal to 0.011 $\mathrm{ms^{-1}}$ (Run-A) and 0.033m $\mathrm{s^{-1}}$ (Run-B). This values give S_t approximately equal to 1.75 for Run-A and 1.17 for Run-B. These values are representative of a non-stationary flow where eddies are generated periodically downstream the obstacle. For experiments in a homogeneous, non rotating flow, $S_t = 0.2$ (Zdravkovich, 1997). This implies that eddies are shed at a lower frequency in these experiments.

figure

3.3　Wind forcing comparison

A unidirectional wind regime, stemming from the north-east (i.e. trade wind), is predominant in both datasets (data not shown). As foreseen, the annually averaged values of the two wind stress datasets have significant differences (Fig. 5). In COADS, the prevailing wind stress intensity is in the range 0.06-0.08 $\mathrm{Nm^2}$; while, in QuikSCAT, the values are much more intense and the prevailing range is 0.10-0.12 $\mathrm{Nm^2}$ (different scales are used in Fig. 5 for a better visualization). Strong differences are observed west of all the island channels, including the Alenuihaha Channel, and also south of the Big Island. COADS forcing, due to its resolution, sees the Hawaiian islands as if the archipelago was continuous and contained only one long and distorted island. Hence the wind stress only accelerates north and south of this unique island. While QuikSCAT forcing captures the effect of each island individually, with an acceleration of the wind stress through the different channels. figure

3.4　Topographic forcing with QuikSCAT wind forcing and no advection

In this experiment, the objective is to analyze the importance of the wind forcing on the Hawaiian oceanic circulation. In sake of simplicity, we take into account only the wind forcing

with the highest resolution : QuikSCAT. **The annually averaged circulation of Run-C (Fig. 3-c) does not show the presence of the NEC. However there is a current similar to the HLCC at** $20.5°N$ **moving progressively towards the south in the lee of the Big Island of Hawaii just between a cyclonic eddy to the north and an anticyclonic one to the south. Circulation in April represents well the behavior of the mesoscale structures (Figure 6).** No vortex shedding is produced in this case. But this circulation is dominated by the presence of two eddies, of opposite vorticity, in the Big Island wake : a cyclonic eddy at the exit of the Alenuihaha Channel, centered at $20°N$, and an anticyclonic eddy south of the Big Island of Hawaii, centered at $18.6°N$. These eddies are intense, with rotational speeds up to 0.4 ms^{-1}, and are stationary all year round. Moreover, we can observe the presence of an anticyclonic eddy present northwest of the Alenuihaha cyclonic eddy at the beginning of its life (Fig. 6-a). This eddy is generated periodically, every 30 to 60 days. It is characterized by a short life-span (10 days). This eddy circles westward around the Alenuihaha cyclonic eddy, moving progressively towards the south (Fig. 6-b/c), and disappears 10 days after its generation (Fig. 6-d).

figure

3.5   QuikSCAT wind forcing with advection and no drag coefficient

In this experiment, the model is forced by the inflow velocity at the eastern open boundary (U_{geo}) and QuikSCAT wind forcing, but the drag coefficient is set equal to zero. **Looking at the annually averaged circulation of Run-D (Fig. 3-d)**, we can note the presence of the NEC in the south and of the HLCC at $19.5 - 20.5°N$. This circulation is characteristic of a circulation in the lee of an archipelago, forming two distinctive zonal area (north and south of $20°N$). The HLCC seems to correspond to the border between cyclonic eddies to the north and anticyclonic eddies to the south. The situation on April 25 (Fig. 7-a) is representative of the whole year circulation except during the months of July and August (Fig. 7-b). **We can remark, as in the annual circulation, a large-scale cyclonic circulation to the north and anticyclonic eddies to the south.** During four months (January to April) these structures expand and move westward. However, during the months of July and August, we observe the successive formation of several eddies. We can note that, during these months, the wind forcing is the strongest of the year (data not shown).

figure

3.6   Topographic and wind forcing with advection

In general the annually averaged circulation of Run-E and Run-F reproduce well the ocean circulation of the study area described in section 1: the NEC splits in two branches when it encounters the Hawaii Archipelago (Fig. 3-e-f). In the wake of the islands the HLCC and the mesoscale eddies

form. **In Run-E, the HLCC is centered around** $20°N$, **while in Run-F this current is shifted to the north closer to the islands** ($20.5°N$). For a more detailed comparison between the two runs, in the following section, we analyze the kinetic energy, the generation and life of the eddies.

In order to analyze the ergodicity, we calculate the total kinetic energy (TKE) at 10-m depth and then the eddy kinetic energy (EKE) in two different ways: EKE_{surf} is the difference between TKE and its surface average $<TKE> = \frac{1}{S} \int_V TKE(x,y,t)dxdy$, while EKE_{time} is the difference between TKE and its monthly time average $\overline{TKE} = \frac{1}{T} \int_0^T TKE(x,y,t)dt$. In this latter calculation, a monthly variability is considered sufficient because, in the study area, there is no significant seasonal variability. For Run-E (data not shown), the higher values of TKE are far from the island, in the meanders of the HLCC. Moreover, EKE_{surf} and EKE_{time} have very similar patterns. For Run-F (data not shown), instead, the highest values of TKE are concentrated in eddies near the islands and again EKE_{surf} and EKE_{time} have similar patterns.

Both cyclonic and anticyclonic are present in the two simulations (Fig. 8). In Run-F the eddies form four zonal areas (Fig. 8-b). Anticyclonic eddies dominate in regions 1 and 3 and cyclonic eddies in regions 2 and 4. In addition, we can notice the presence of small eddies at $19.5°N$ in Run-F (Fig. 8-b). These eddies are characterized by a length scale similar to the Alenuihaha Channel width. Structures from Run-E are less intense and defined than the ones from Run-F. The cyclonic minimum value of relative vorticity is equal to $-2.46 \ 10^{-5}$ s^{-1} in May for the Run-E and to $-4.35 \ 10^{-5}$ s^{-1} in November for the Run-F. The anticyclonic maximum value of relative vorticity is equal to $+2.37 \ 10^{-5}$ s^{-1} in August for Run-E and to $+4.12 \ 10^{-5}$ s^{-1} in December for Run-F. Indeed, the anticyclonic relative vorticity values are generally twice higher for Run-F than Run-E.

After their formation, the eddies generally move westward. In general, we observed that the cyclones move toward the north-west and anticyclones to the south-west. This fact has been explained by Cushman-Roisin (1994) in terms of potential vorticity conservation on a β-plane and then observed in satellite data by Morrow et al. (2004). Rather than to interpret the westward drift in terms of potential vorticity, Cushman-Roisin (1994) also explain the drift by a balance of forces. **Moreover we observe a southward movement of the cyclonic eddies during the first time of their life. Patzert (1969), Lumpkin (1998), Seki et al. (2002) and Dickey et al. (2008) have also reported cyclonic eddies moving southward before translating west-northwestward.** This phenomenon can cause a disturbance in the flow field with cyclones (anticyclones) present in the northern (southern) part of the wake. That process is well observed in the Run-F results, where the anticyclones are better defined than in Run-E.

figure

3.7 Features of the cyclones

Specific numerical cyclones are chosen**, during the last five years of each simulation,** because they are spatially and temporally representative of cyclone *Opal* studied during the cruise E-FLUX III (March 10-28, 2005). These eddies are compared with each other and with observational data. **The different eddy characteristics' statistics and the ones of** cyclone *Opal* are summarized in the Table 2. Cyclones are expected to exhibit an uplift of isopycnal and of isothermal surfaces. Depending on the runs, these characteristics are more or less apparent (Fig. 9, Fig. 10). The sections reveal an intense doming of isothermal and isopycnal surfaces with outcropping at the surface for Run-C and Run-F (Fig. 9-c, Fig. 10-c). This uplift is also present for Run-A, Run-D and Run-E (Fig. 9-a, Fig. 10-a/b) but is not as pronounced as in the previous results. The Run-B results are characterized by smooth isothermal and isopycnal surfaces (Fig. 9-b). **The deepest depths, where the eddies still influence the isopycnals, vary between** 90 **m (Run-B) and** 250 **m (Run-A, Run-C, Run-F). We have calculated an estimate of the diameter of the different cyclonic eddies following the method used by Dickey et al. (2008). These diameters vary between** 160 **km (Run-A) and** 210 **km (Run-C, Run-D). The diameters for Run-E and Run-F features are of the same order than the one of cyclone *Opal*. The values of the maximum tangential velocities (Table 2) can give us information on the intensity of each cyclones. The Run-A and Run-B results are characterized by the lowest velocity** $(0.23-0.24 \text{ ms}^{-1})$**, while those of Run-C, Run-D and Run-F by the highest velocity** $(0.53-0.55 \text{ ms}^{-1})$**. An intermediate value is found for the Run-E results** (0.30 ms^{-1})**.**

figure

figure

table

The numerical cyclones of Run-A and Run-B are not energetic enough and those of Run-C and Run-D are too large compared to the characteristics of cyclone *Opal*. Hence the results of Run-E and Run-F are the closest ones to the *Opal* characteristics. Hereafter we concentrate on these two runs **during the tenth year of simulation.** We have calculated the east-west (north-south) components of the horizontal velocity vector along a north-south (east-west) transect for Run-E and Run-F. We report zonal and meridional components of the 40-m depth horizontal velocity along meridional and zonal transect, respectively, for eddies *C5-E* and *C1-F* in Fig. 11. We have chosen this depth for a comparison with in situ measurements performed by Nencioli et al. (2008) inside the cyclone *Opal*.

The position of the center of the eddy can be located at the point of minimal velocity, here near $19.5°N$, $156.6°W$ for both eddies (Fig. 12). figure

figure

In Fig. 13 we show the distribution of the zonal and meridional components of the 40-m depth horizontal velocity with respect to the distance from the eddy center for both *C5-E* (Run-E, April 13) and *C1-F* (Run-F, March 28). Both eddies are characterized by values that increase linearly with distance from the center until peaking and then slowly decaying. For *C5-E*, the peak value is about 0.35 ms^{-1}, while it nearly reaches 0.60 ms^{-1} for *C1-F*. The linear part corresponds to the solid-body rotation core of the eddy. Otherwise, both eddies appear quite asymmetric and stretched. Hence it is difficult to define with precision an eddy radius. Nonetheless, it appears clearly that the part in solid body rotation has a diameter smaller than the one estimated above, following Dickey et al. (2008).

figure

4 Discussion

A series of numerical simulations on the Hawaiian region has been done in order to examine the relative importance of wind and topographic forcing on the general circulation and the generation of the eddies. Depending on the runs, the general pattern of the regional oceanic circulation by Lumpkin (1998) is more or less respected. **The ocean circulations generated by the model forced by the topographic forcing with the inflow currents and no wind (Run-A, Run-B) do not match with this regional circulation. Moreover, these circulations are not realistic because the intensity of the eddies is too low** $(0.23-0.24 \text{ ms}^{-1})$**.** Both simulations show the importance of inflow current and topographic forcing on oceanic eddy shedding. When the model is forced only by QuickSCAT wind data (Run-C), two stationary eddies and a periodical one develop in the island wake, responding to the vorticity injected by the wind stress curl. **The fact that the cyclone is stationary could be due to topographic β-effect (Cushman-Roisin and Beckers, September 2011). Hence in our case, the cyclone will tend to move toward the north-east against the islands of Maui and the Big Island. As for the anticyclonic eddy, its position inside the domain so close to the boundary prevents us to be confident about its behavior. Nevertheless comparing Run-C with Run-D and Run-F (Table 1) the absence of inflow as boundary condition, and hence the absence of NEC, seems to be the reason preventing the westward drift of the anticyclonic eddy. The ocean circulation generated by the model forced by QuickSCAT, but without drag coefficient (Run-D), complies with the circulation of Lumpkin (1998) but with larger eddies than the realistic ones.** It implies that the effect of a drag coefficient leads to the compactness of the structures. Nevertheless, in July and August, several intense eddies have been generated in Run-D. During this period, wind forcing is the strongest of the year and acts as a trigger mechanism even when the drag coefficient is set to zero. **The ocean circulations generated by the model**

	Run-A	Run-B	Run-C	Run-D	Run-E	Run-F	*Opal*
Isopycnal outcropping	$\sigma_{t_{23.6}}$	$\sigma_{t_{23.6}}$	$\sigma_{t_{23.6}}$	$\sigma_{t_{23.6/23.8}}$	$\sigma_{t_{23.6/23.8}}$	$\sigma_{t_{23.6/23.8}}$	$\sigma_{t_{23.6}}$
Depth impact (m)	> 250	90 ± 50	> 250	240 ± 20	130 ± 70	> 250	> 250
Diameter (km)	160 ± 10	n.d.	210 ± 20	210 ± 10	180 ± 20	180 ± 30	180-200
Velocity (ms^{-1})	0.24 ± 0.04	0.23 ± 0.02	0.54 ± 0.12	0.55 ± 0.05	0.3 ± 0.05	0.53 ± 0.09	0.6

Table 2. Features of the cyclones based on statistics for the last 5 years of each simulation and for *Opal* (n.d. stands for not determined).

forced by COADS (Run-E) and QuickSCAT data (Run-F) agree with the known circulation. The annually averaged large-scale circulation is roughly composed of cyclonic eddies to the north and anticyclonic eddies to the south, separated by the HLCC. **This is due to the fact that wind, inflow current and topographic forcings act together leading to the same effect.** Indeed these three forcings have a cumulative effect while each forcing, taken independently, is not able to create the known circulation. This fact is in agreement with the experiments of Jiménez et al. (2008) applied to the case of eddies shed by the island of Gran Canaria. **Nevertheless the study of mesoscale structures in Run-F, based on snapshots (3-days averaged), reveals the splitting of the lee of the Hawaiian Island into four zonal areas from south to north characterized by the alternating presence of anticyclonic and cyclonic eddies. This is not revealed in the regional circulation observed by Lumpkin (1998). The resolution of the dataset considered by Lumpkin (1998) may not be sufficient to reproduce the details of these circulation features. Moreover, in our case, we observe that the generation of cyclonic eddies at the northwestern tip of the Big Island is rare (Run-F). Hence we agree with Yoshida et al. (2010) affirming that both positive and negative SSH eddy signals are generated southwest of the Big Island. Nevertheless Karman vortex street stays a viable eddy generation mechanism for the lee of the Hawaiian archipelago.** Significant differences appear between Run-E and Run-F and have to be noted. A higher temporal variability of the kinetic energy appears clearly in Run-F with respect to Run-E. Since both simulations seem to satisfy the ergodic hypothesis, we think that this temporal variability is induced by the higher spatial variability of the QuickSCAT wind forcing. Indeed, the similarity between EKE and TKE, in both Run-E and Run-F, indicates that most of the wind forcing momentum feeds mesoscale phenomena and that the high values of TKE in the lee of the islands are locally generated. In agreement with Calil et al. (2008), our model results show that having good spatial resolution for the surface momentum forcing is vital to produce realistic levels of kinetic energy and vorticity in the ocean circulation. With respect the $\frac{1}{4}^{\circ}$ QuickSCAT climatology, the $\frac{1}{2}^{\circ}$ COADS one does not produce the wind acceleration through the Alenuihaha Channel and other passages between islands.

In the same area, period and conditions of the E- Flux III field campaigns (i.e. in March and April, downwind of the Alenuihaha Channel and during strong, persistent northeasterly trade winds), our model generates cyclonic eddies in all the simulations. Concerning in situ data, the eddy *Opal*, an intense feature, was likely in a well-developed segment of its lifetime when it was measured with a diameter of 180-200 km and a maximum velocity of around 0.6 ms^{-1} at a radial distance of roughly 20-30 km. It also exhibited a vertical isothermal uplift with some isopycnes apparently outcropping to the surface (Dickey et al., 2008). We then compare the modeled cyclonic cold-core eddies with respect to the observations of the eddy *Opal*. For Run-A and Run-B, both cyclones show an outcropping of the isopycne $\sigma_{t_{23.6}}$ to the surface. But the uplift of the isotherms is more pronounced in Run-A than in Run-B. This fact can be explained by a homogenization when the current is more intense. For Run-C, the wind stress curl causes the development of cyclonic eddies by forcing strong Ekman pumping, which leads to water upwelling. The isothermal and isopycnal uplift is the strongest of the six simulations. Because of the Ekman pumping, it is possible that the wind forcing has a greater impact upon the strength of the upwelling in the immediate lee region, as suggested by Yoshida et al. (2010). We have concentrated on the two cyclonic eddies of Run-E and Run-F because they correspond to the most realistic simulations. The model reproduces well the intense doming of isothermal and isopycnal associated with the cyclonic structures. Calil et al. (2008) said that the model forced by COADS climatology did not produce significant isolated mesoscale cyclonic eddies. In our model, Run-E cyclones are produced but appear smaller in diameter and less energetic than Run-F ones and *Opal*. Moreover the maximum velocity in Run-F cyclones are higher than the Run-E one and closer in amplitude to the maximum velocities measured in *Opal* (Nencioli et al., 2008). The behavior of the simulated cyclonic eddy is similar to that observed, but the southward drift of *Opal* is well reproduced only by *C1-F*.

5 Conclusions

The Hawaiian archipelago has a strong influence on both the atmospheric and the oceanic circulations. In this study, we performed several experiments to study the relative importance of topographic and wind forcing on oceanic eddy shedding by the Hawaiian archipelago. We have compared the oceanic circulation around Hawaii and have obtained significant differences between the simulations using different

forcings. This study demonstrates the need for the presence of the three forcings (wind, inflow current and topography) to reproduce the oceanic circulation. These forcings have a cumulative effect on the generation of mesoscale eddies and lead to a complex oceanic circulation pattern. While each forcing, taken independently, is not able to create the known circulation. The wind stress curl, via the Ekman pumping mechanism, has also been identified as an important mechanism upon the strength of the upwelling in the immediate lee region. In order to well reproduce the oceanic circulation in the area, it is necessary to have, not only a high spatial resolution for the circulation model, but also a wind stress forcing data that reproduces the complexity of the atmospheric flow between the islands. In agreement with previous numerical studies, our results suggest that a higher spatial resolution allows to reproduce more realistic circulation. In particular, the simulation forced by QuikSCAT wind data (Run-F) reproduces well the energetic mesoscale structures observed during the E-Flux field experiments (Dickey et al., 2008), including their hydrological characteristics and behavior. This setup will allow future studies that are needed to better understand the role of temporal variability on the behavior of mesoscale eddies and the role of these structures in the distribution of biogeochemical properties.

References

Aristegui, J., Sangra, P., Henandez-Leon, S., Canton, M., and Hernandez-Guerra, A.: Island-induced eddies in the Canary Islands, Deep-Sea Res. I, 41, 1509–1525, 1994.

Aristegui, J., Tett, P., Hernandez-Guerra, A., Basterretxea, G., Montero, M. F., Wild, K., Sangra, P., Hernandez-Leon, S., Canton, M., Garcia-Braun, J. A., Pacheco, M., and Barton, E. D.: The influence of island-generated eddies on chlorophyll distribution: a study of mesoscale variation around Gran Canaria, Deep-Sea Res. I, 44, 71–96, 1997.

Barton, E., Basterretxea, G., Flament, P., Mitchelson-Jacob, E., Jones, B., Aristegui, J., and Herrera, F.: Lee region of Gran Canaria, J. Geophys. Res., 105, 17 173–17 193, 2000.

Beckmann, A. and Haidvogel, D.: Numerical simulation of flow around a tall isolated seamount. Part 1: Problem formulation and model accuracy, J. Phys. Oceanogr., 23(8), 1736–1753, 1993.

Bidigare, R. R., Benitez-Nelson, C., Leonard, C. L., Quay, P. D., Parsons, M. L., Foley, D. G., and Seki, M. P.: Influence of a cyclonic eddy on microheterotroph biomass and carbon export in the lee of Hawaii, Geophys. Res. Lett., 30, 1318, doi:10.1029/2002GL016393, 2003.

Blanke, B., Speich, S., Bentamy, A., Roy, C., and Sow, B.: Modeling the structure and variability of the southern Benguela upwelling using QuikSCAT wind forcing, J. Geophys. Res., 110, C07018, doi:10.1029/2004JC002529, 2005.

Calil, P. H. R., Richards, K. J., Yanli, J., and Bidigare, R. R.: Eddy activity in the lee of the Hawaiian Islands, Deep-Sea Res. II, 55, 1179–1194, 2008.

Callahan, P. S. and Lungu, T.: QuikSCAT Science Data Product User's Manual (v3.0), Tech. rep., Jet Propul. Lab., Pasadena, CA, 91 pp., 2006.

Chavanne, C., Flament, P., Lumpkin, R., Dousset, B., and Bentamy, A.: Scatterometer observations of wind variations induced by oceanic islands: implications for wind-driven ocean circulation., Can. J. Remote Sens., 28, 466–474, 2002.

Chelton, D. B., deSzoeke, R. A., Schlax, M. G., El Naggar, K., and Siwertz, N.: Geographical variability of the first-baroclinic Rossby radius of deformation, J. Phys. Oceanogr., 28, 433–460, 1998.

Cherniawsky, J. Y. and Crawford, W. R.: Comparison between weather buoy and Comprehensive Ocean-Atmosphere Data Set wind data for the west coast of Canada, J. Geophys. Res., 101, 18 377–18 390, 1996.

Cushman-Roisin, B.: Introduction to Geophysical Fluid Dynamics, Prentice Hall, 1994.

Cushman-Roisin, B. and Beckers, J. M.: Introduction to Geophysical Fluid Dynamics : Physical and Numerical Aspects, Under contract with Academic Press, 2011.

Da Silva, A. M., Young, C. C., and Levitus, S.: Atlas of surface marine data 1994, vol. 1, algorithms and procedures, Tech. rep., U. S. Department of Commerce, NOAA, 1994.

Dickey, T. D., Nencioli, F., Kuwahara, V. S., Leonard, C., Black, W., Rii, Y. M., Bidigare, R. R., and Zhang, Q.: Physical and bio-optical observations of oceanic cyclones west of the island of Hawaií, Deep-Sea Res. II, 55, 1195–1217, 2008.

Dong, C. and McWilliams, J. C.: A numerical study of island wakes in the Southern California Bight, Cont. Shelf Res., 27, 1233–1248, doi:10.1016/j.csr.2007.01.016, 2007.

Dong, C., Mavor, T., Nencioli, F., Jiang, S., Uchiyama, Y., McWilliams, J. C., Dickey, T. D., Ondrusek, M., Zhang, H., and Clark, D. K.: An oceanic eddy on the lee side of Lanai Island, Hawai'i, J. Geophys. Res., 114, C10008, doi:10.1029/2009JC0053467, 2009.

Firing, Y. L. and Merrifield, M. A.: Extreme sea level events at Hawaii : Influence of mesoscale eddies, Geophys. Res. Lett., 31, L24306, doi:10.1029/2004GL021539, 2004.

Jiménez, B., Sangrà, P. and Mason, E.: A numerical study of the relative importance of wind and topographic forcing on oceanic eddy shedding by tall, deep water islands., Ocean Model., 22, 146–157, doi:10.1016/j.ocemod.2008.02.004, 2008.

Lumpkin, C. F.: Eddies and currents in the Hawaii islands, Ph.D. thesis, University of Hawaii, 1998.

Marchesiello, P., McWilliams, J. C., and Shchepetkin, A.: Open boundary condition for long-term integration of regional oceanic models, Ocean Model., 3, 1–21, doi:10.1016/S1463-5003(00)00013-5, 2001.

Monaldo, F. M., Thompson, D. R., Pichel, W. G., and Clemente-Colon, P.: A systematic comparison of QuikSCAT and SAR ocean surface wind speeds, IEEE T. Geosci. Remote, 42, 283–291, 2004.

Morrow, R., Birol, F., Griffin, D., and Sudre, J.: Divergent pathways of cyclonic and anti-cyclonic ocean eddies, Geophys. Res. Lett., 31, L24311, doi:10.1029/2004GL020974, 2004.

Nencioli, F., Kuwahara, V. S., Dickey, T. D., Rii, Y. M., and Bidigare, R. R.: Physical dynamics and biological implications of a mesoscale eddy in the lee of Hawai'i : Cyclone Opal observations during E-FLUX III, Deep-Sea Res. II, 55, 1252–1274, 2008.

Patzert, W. C.: Eddies in Hawaiian Islands, Tech. rep., Hawaii Institute og Geophysics, University of Hawaii, 1969.

Penven, P., Cambon, G., Tan, T. A., Marchesiello, P., Debreu, L.: ROMSTOOLS user guide, Tech. rep., Inst. de Rech. pour le Dév., Marseille, France, http://roms.mpl.ird.fr, 2010.

Penven, P., McWilliams, J. C., Marchesiello, P., and Chao, Y.: Coastal Upwelling response to atmospheric wind forcing along the Pacific coast of the United States, Ocean Sciences Meeting, Honolulu, Hawaii (USA), 2002.

Qiu, B., Koh, D. A., Lumpkin, C., and Flament, P.: Existence and formation mechanism of the North Hawaiian Ridge Current, J. Phys. Oceanogr., 27, 431–444, 1997.

Renfrew, I. A., Petersen, G. N., Sproson, D. A. J., Moore, G. W. K., Adiwidjaja, H., Zhang, S., and North, R.: A comparison of aircraft-based surface-layer observations over Denmark Strait and the Irminger Sea with meteorological analyses and QuikSCAT winds, Q. J. Roy. Meteor. Soc., 135, 2046–2066, 2009.

Seki, M. P., Polovina, J. J., Brainard, R. E., Bidigare, R. R., Leonard, C. L., and Foley, D. G.: Biological enhancement at cyclonic eddies tracked with GOES thermal imagery in Hawaiian waters, Geophys. Res. Lett., 28, 1583–1586, 2001.

Seki, M. P., Lumpkin, R., and Flament, P.: Hawaii cyclonic eddies and blue marlin catches: the case study of the 1995 Hawaiian International Billfish Tournament, J. Oceanogr., 58, 739–745, 2002.

Shchepetkin, A. F. and McWilliams, J. C.: A method for computing horizontal pressure-gradient force in an oceanic model with nonaligned vertical coordinate, J. Geophys. Res., 108, 3090, doi: 10.1029/2001JC001047, 2003.

Shchepetkin, A. F. and McWilliams, J. C.: The regional oceanic modeling system (ROMS): a split-explicit, free-surface, topography-following-coordinate oceanic model, Ocean Model., 9, 347–304, doi:10.1016/j.ocemod.2004.08.002, 2005.

Smith, R. B. and Grubisic, V.: Aerial observations of Hawaii's wake, J. Atmos. Sci., 50, 3728–3750, 1993.

Smith, W. H. F. and Sandwell, D. T.: Global sea floor topography from satellite altimetry and ship depth soundings, Science, 227, 1956–1962, doi:10.1126/science.277.5334.1956, 1997.

Wu, R. and Xie, S.: On Equatorial Pacific surface wind changes around 1977: NCEP-NCAR reanalysis versus COADS observations , J. Clim., 16, 167–173, 2003.

Xie, S., Liu, W., Liu, Q., and Nonaka, M.: Far-Reaching Effects of the Hawaiian Islands on the Pacific Ocean-Atmosphere System, Science, 292, 2057–2060, 2001.

Yoshida, S., Qiu, B., and Hacker, P.: Wind-generated eddy characteristics in the lee of the island of Hawaii, J. Geophys. Res., 115, C03019, doi:10.1029/2009JC005417, 2010.

Zdravkovich, M. M.: Flow around Circular Cylinders: A Comprehensive Guide through Flow Phenomena, Experiments, Applications, Mathematical Models, and Computer Simulations, Oxford University Press, 694 pp., 1997.
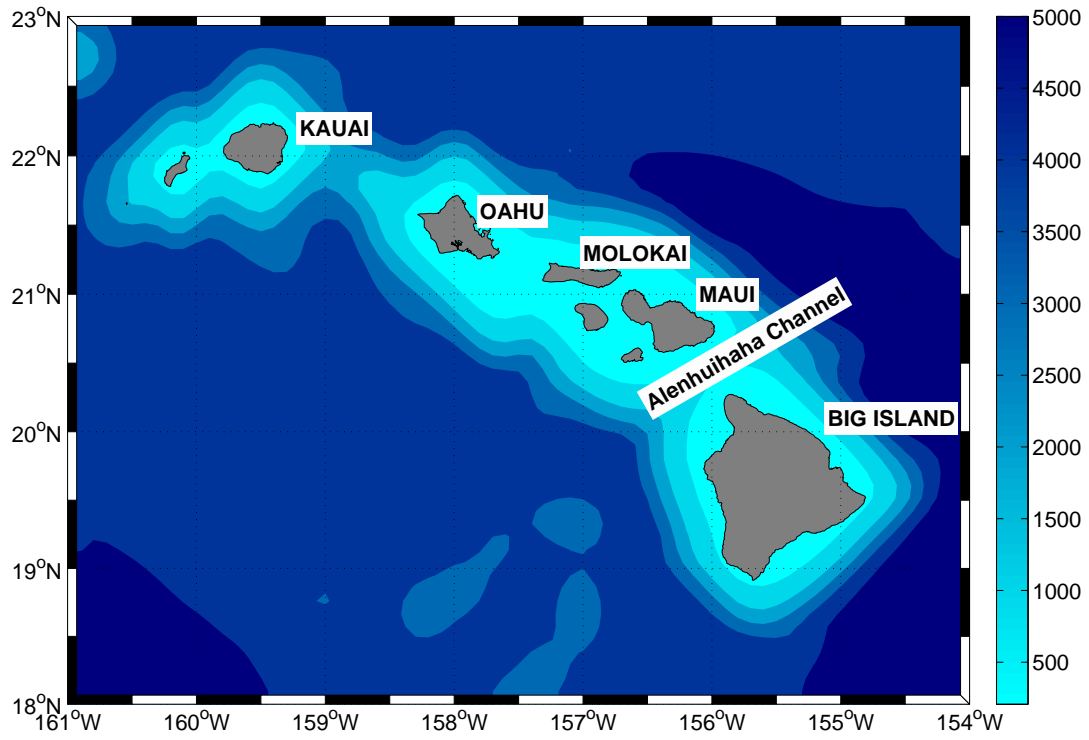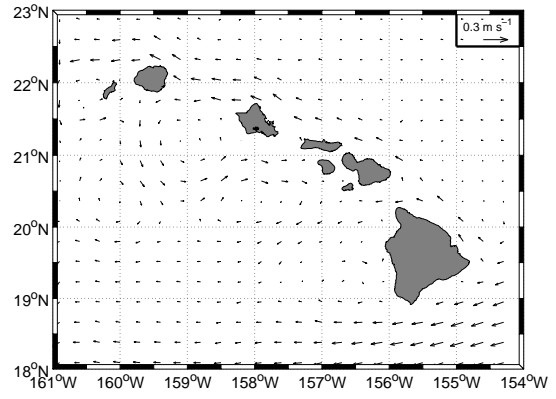
Fig. 1. Model domain and bathymetry [m]. Names of the islands and coastline at higher resolution are reported for geographical information.
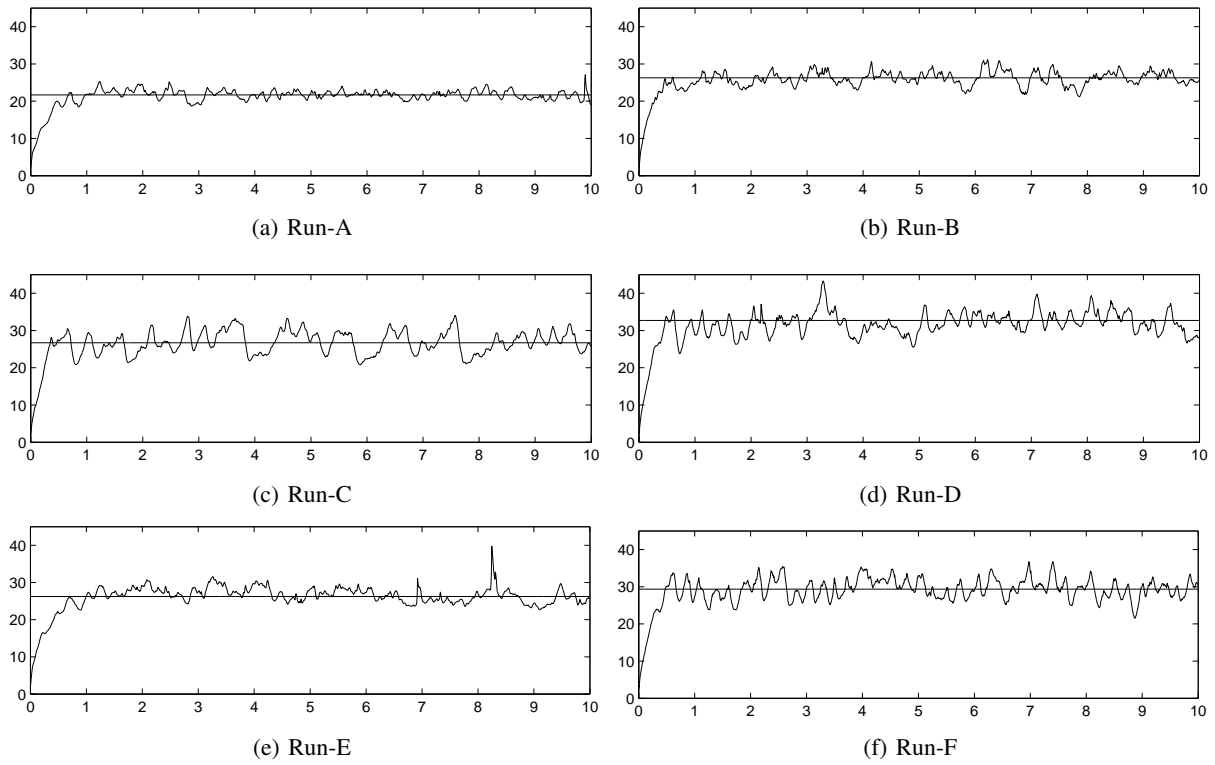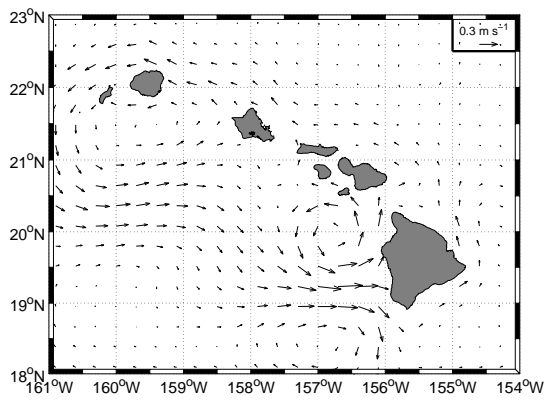
Fig. 2. Temporal evolutions (model time, years) of volume-averaged kinetic energy [cm^2s^{-2}] for the six numerical experiments. The horizontal lines indicate the 10-year mean values.
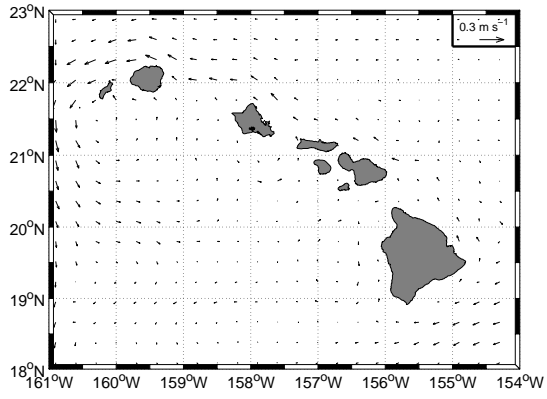
(a) Run-A

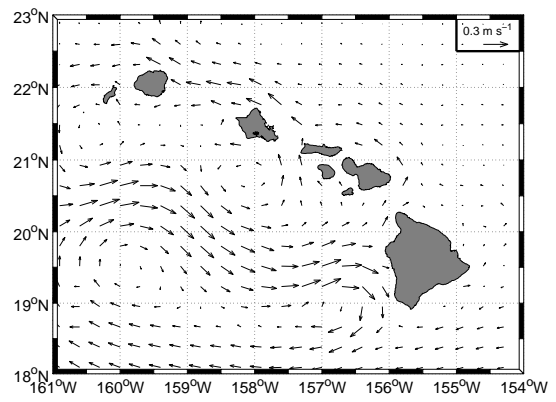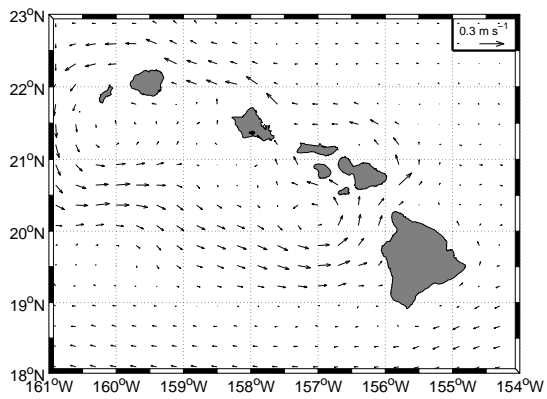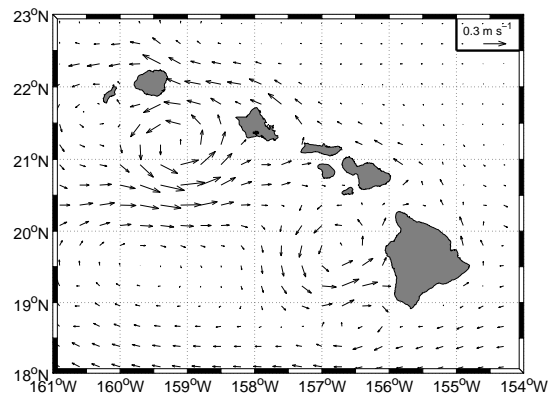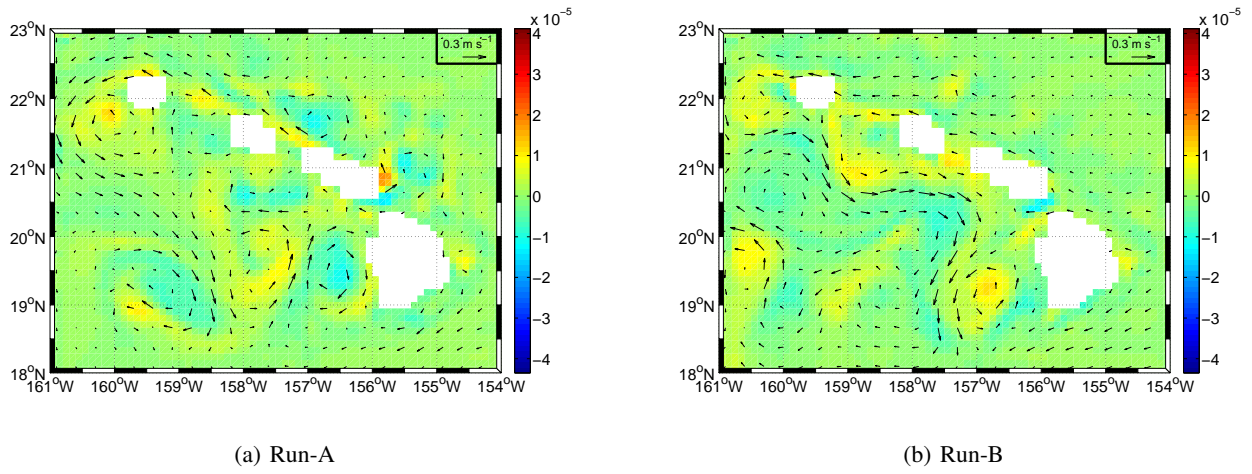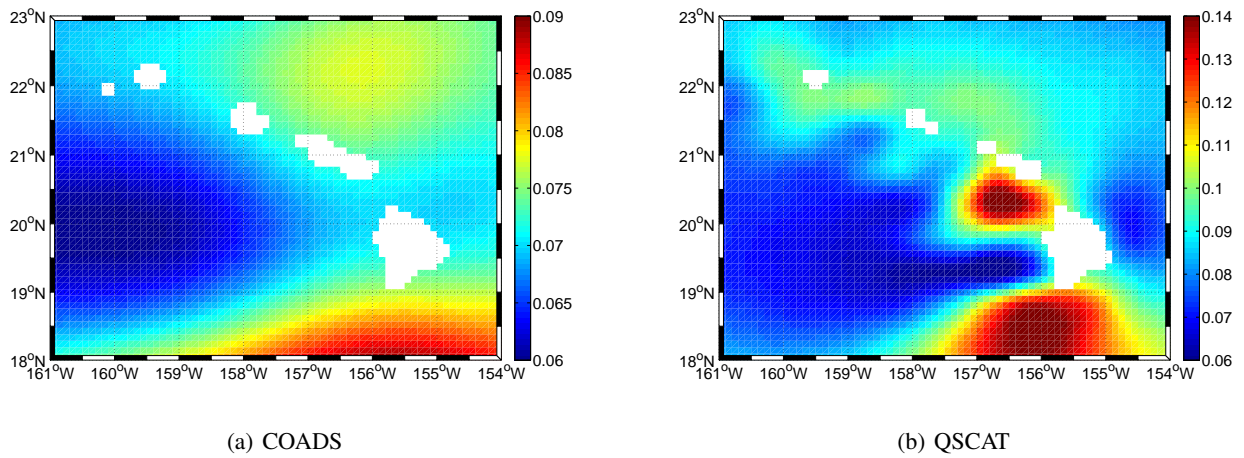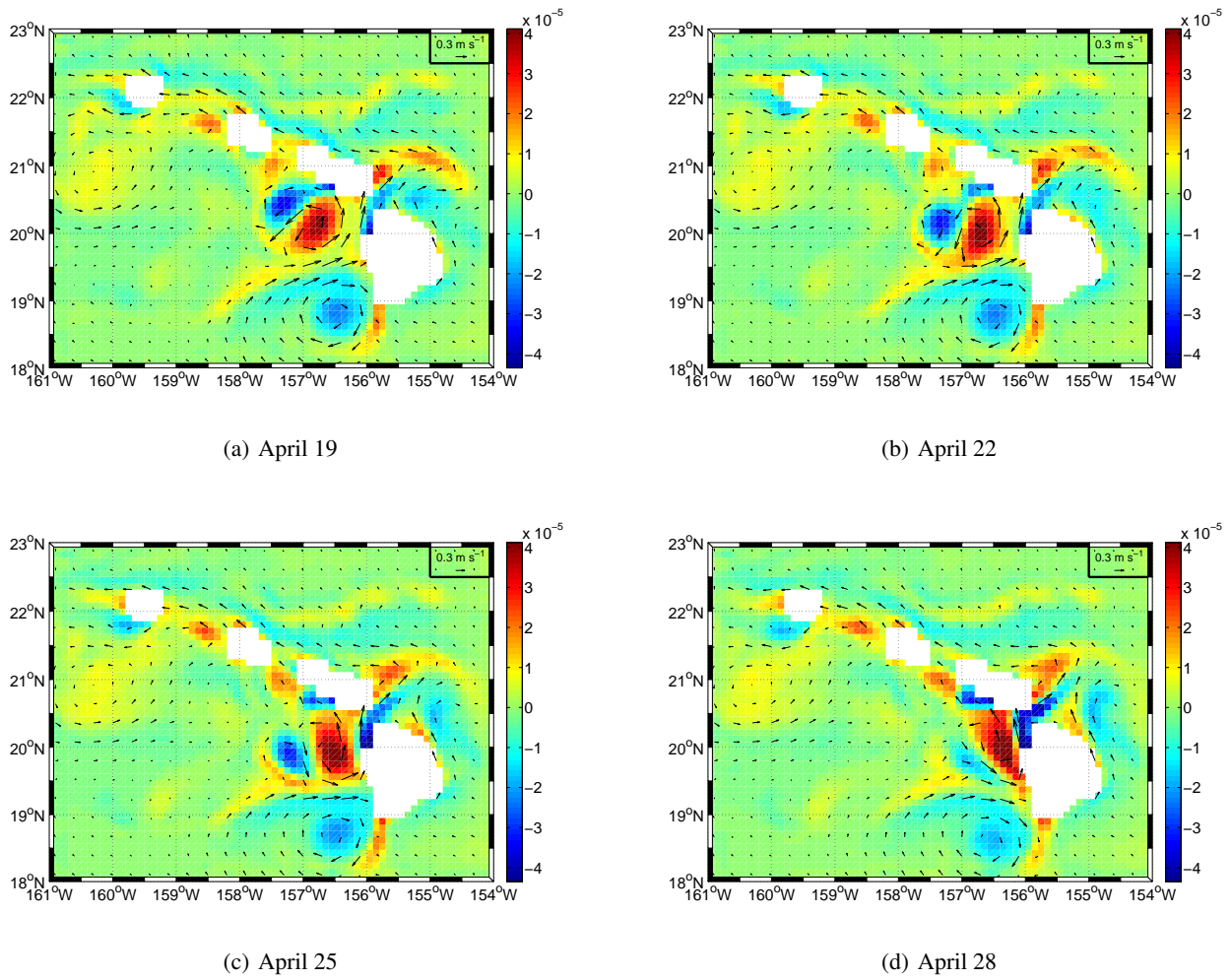(b) Run-B

(c) Run-C

(d) Run-D

(e) Run-E

(f) Run-F

**Fig. 3.** Annually-averaged currents' velocity vectors at 40-m depth.

(a) Run-A

(b) Run-B

Fig. 4. Relative vorticity field with velocity vectors at 10-m depth on August 22 for Run-A (left) and Run-B (right).

(a) COADS

(b) QSCAT

Fig. 5. Annually-averaged wind stress values [Nm^{-2}]. Different scales are used for a better visualization.

(a) April 19

(b) April 22

(c) April 25

(d) April 28

Fig. 6. Relative vorticity field and velocity vectors for Run-C at 10-m depth at different dates in April.
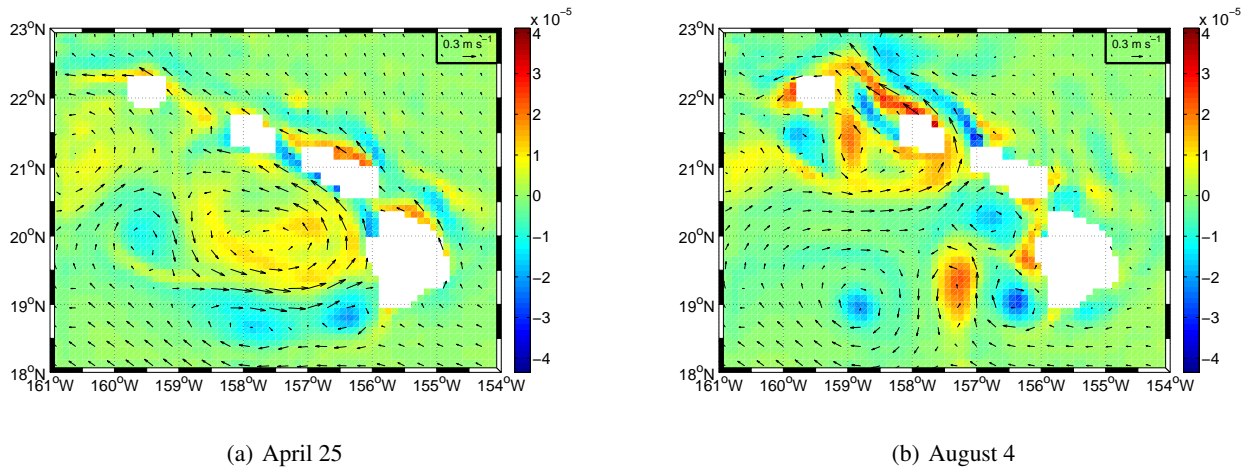
(a) April 25

(b) August 4

Fig. 7. Relative vorticity field and velocity vectors at 10-m depth on April 25 (left) and August 4 (right) for Run-D.

(a) Run-E

(b) Run-F
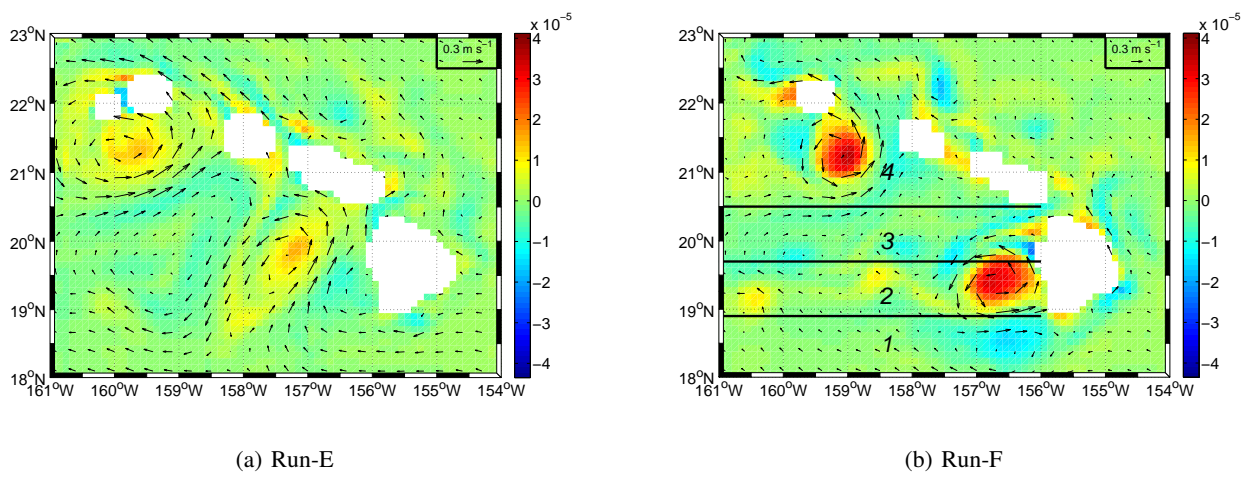
Fig. 8. Relative vorticity field with velocity vectors at 10-m depth on August 25 for Run-E (left) and Run-F (right). In Run-F, anticyclonic eddies dominate in regions 1 and 3 and cyclonic eddies in regions 2 and 4.
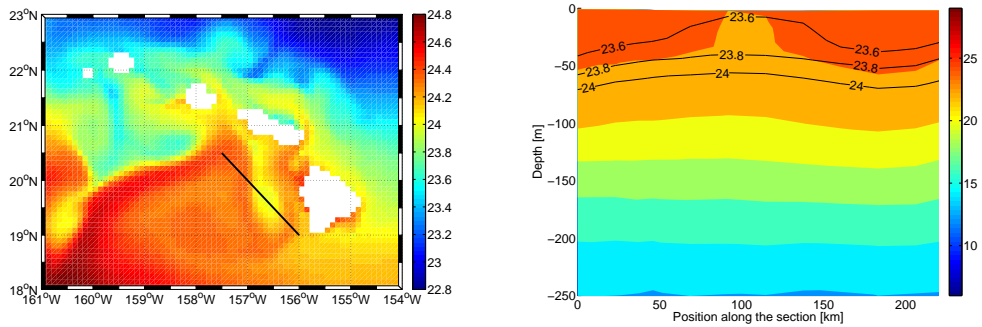
(a) C3-A
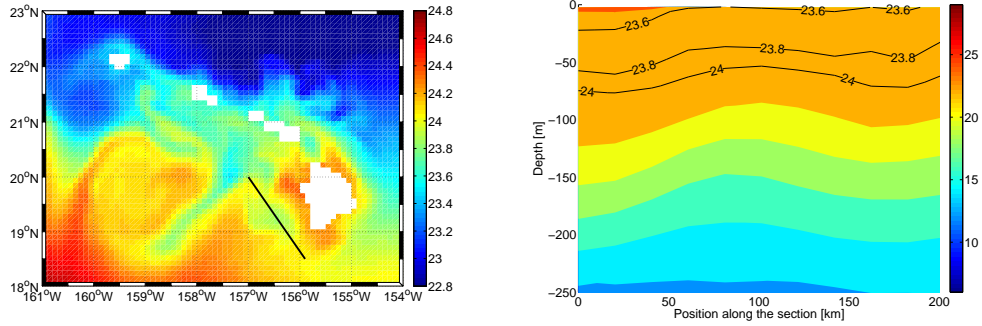
(b) C3-B
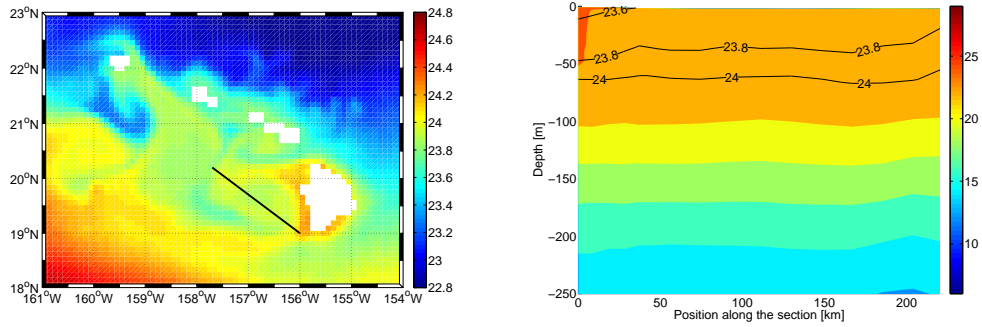
(c) C2-C
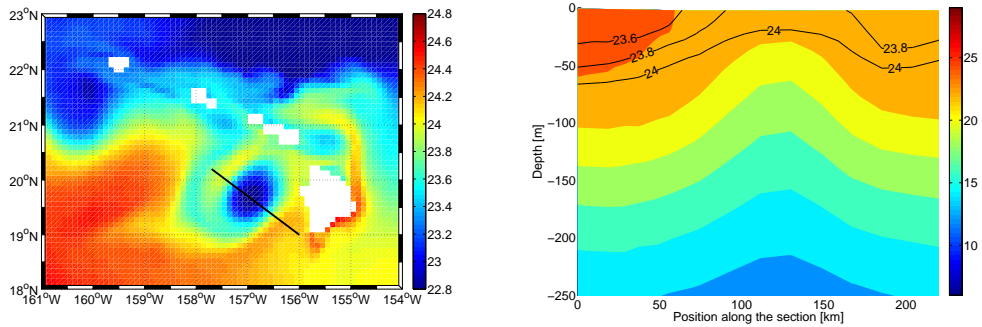
Fig. 9. Left : surface temperature maps on March 28 with position of the transects (black straight line) crossing the center of a cyclonic eddy Run-A (top), Run-B (middle) and Run-C (bottom). Right : Corresponding vertical sections of temperature. The black lines in the vertical sections represent $\sigma_{t_{23.6}}$, $\sigma_{t_{23.8}}$ and $\sigma_{t_{24}}$ isopycnals.
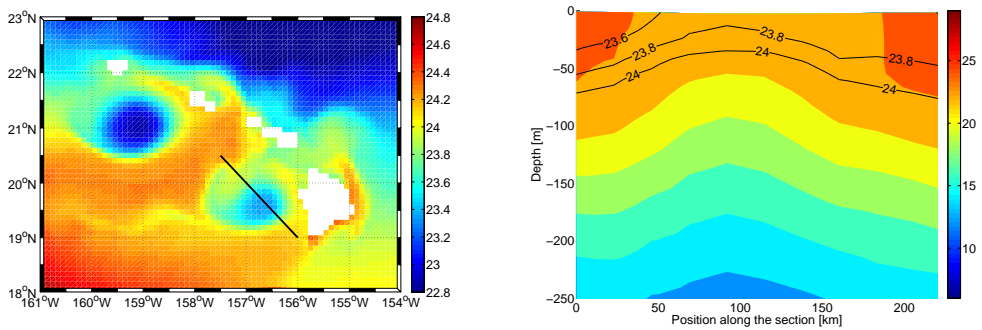
(a) C3-D
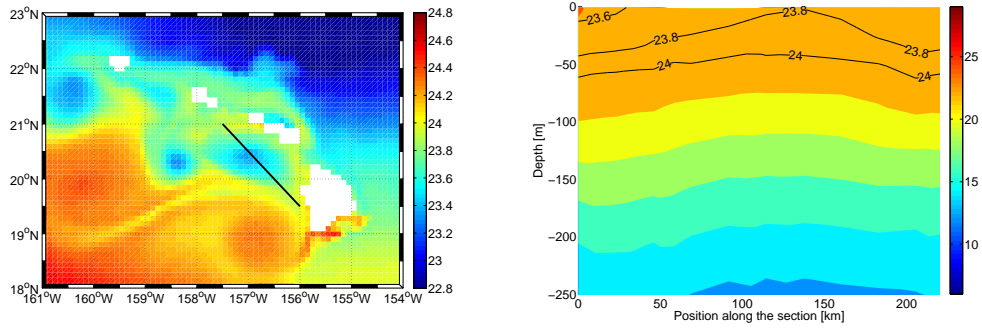
(b) C5-E

(c) C1-F

Fig. 10. Left : surface temperature maps with position of the transects (black straight line) crossing the center of a cyclonic eddy on April 13 for Run-E (middle) and on March 28 for both Run-D (top) and Run-F (bottom). Right : Corresponding vertical sections of temperature. The black lines in the vertical sections represent $\sigma_{t_{23.6}}$, $\sigma_{t_{23.8}}$ and $\sigma_{t_{24}}$ isopycnals.

(a) Run-E   (b) Run-F
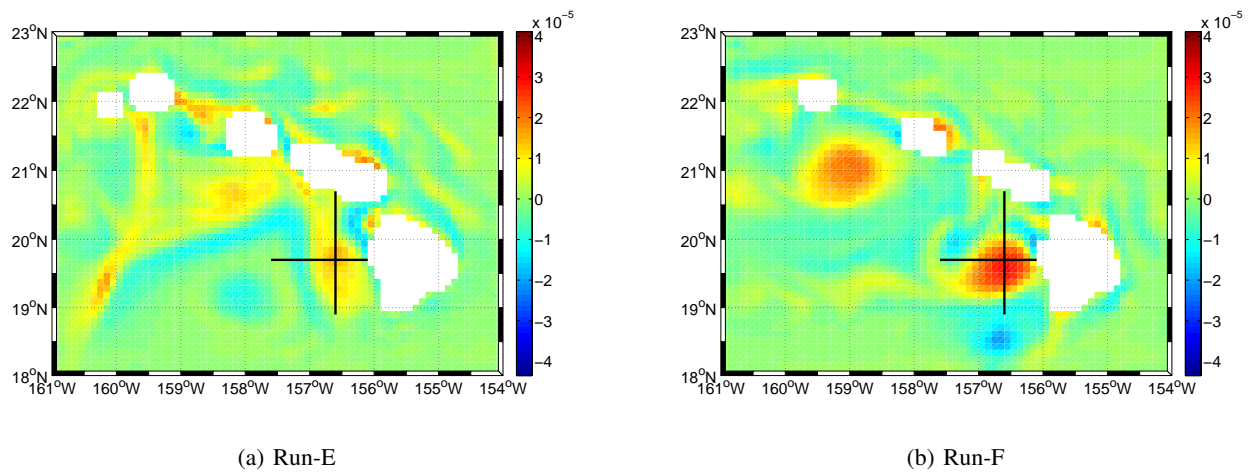
Fig. 11. Relative vorticity field at 40-m depth with position of the transects (black straight line) of the eddy *C5-E* (Run-E, April 13, left) and of the eddy *C1-F* (Run-F, March 28, right).

(a) Run-E (b) Run-F
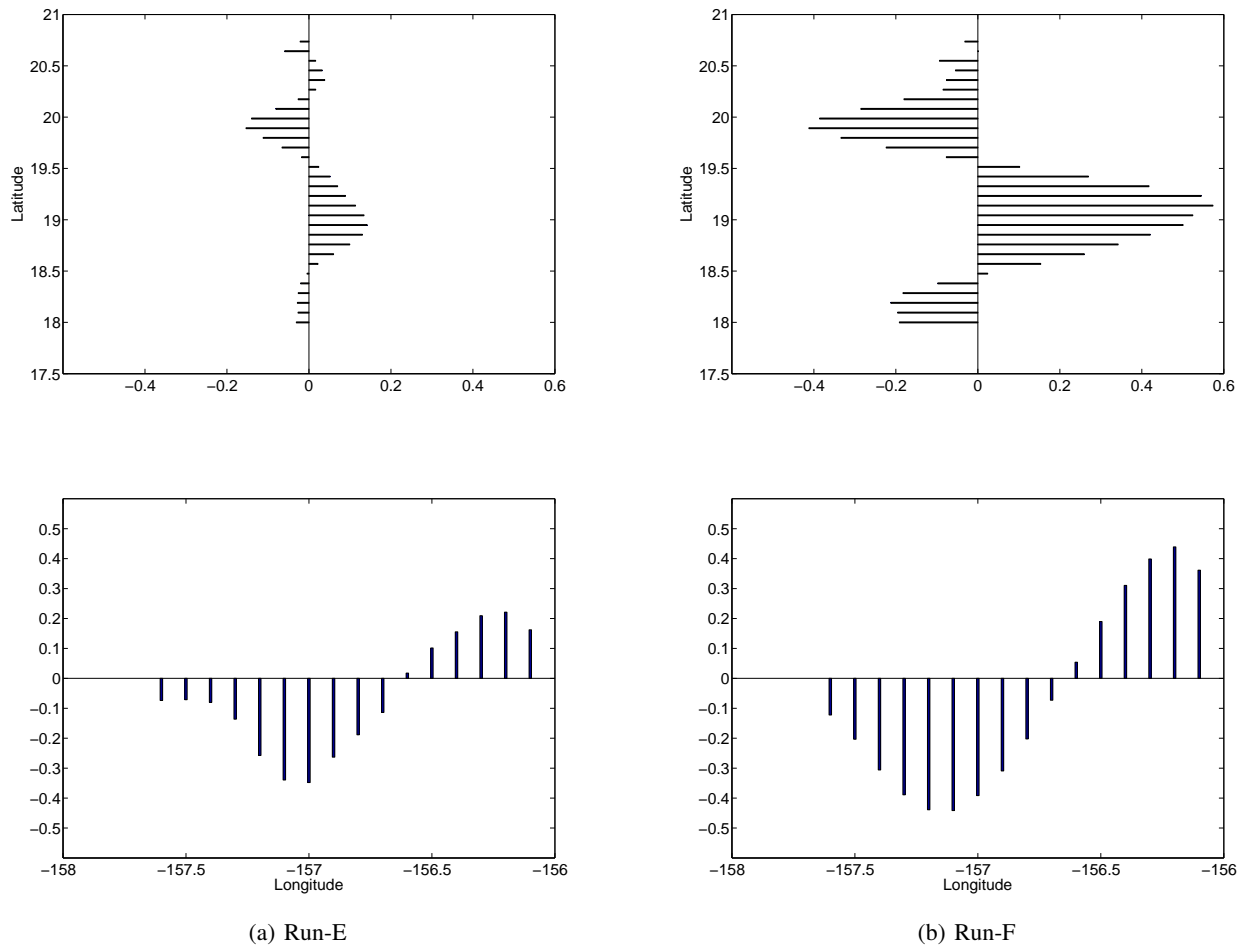
Fig. 12. East-west horizontal velocity [m s^{-1}] component at 40-m depth vector across a north-south transect (top) and north-south horizontal velocity component across a east-west transect (bottom) of the eddy *C5-E* (Run-E, April 13, left) and of the eddy *C1-F* (Run-F, March 28, right).

(a) Run-E   (b) Run-F
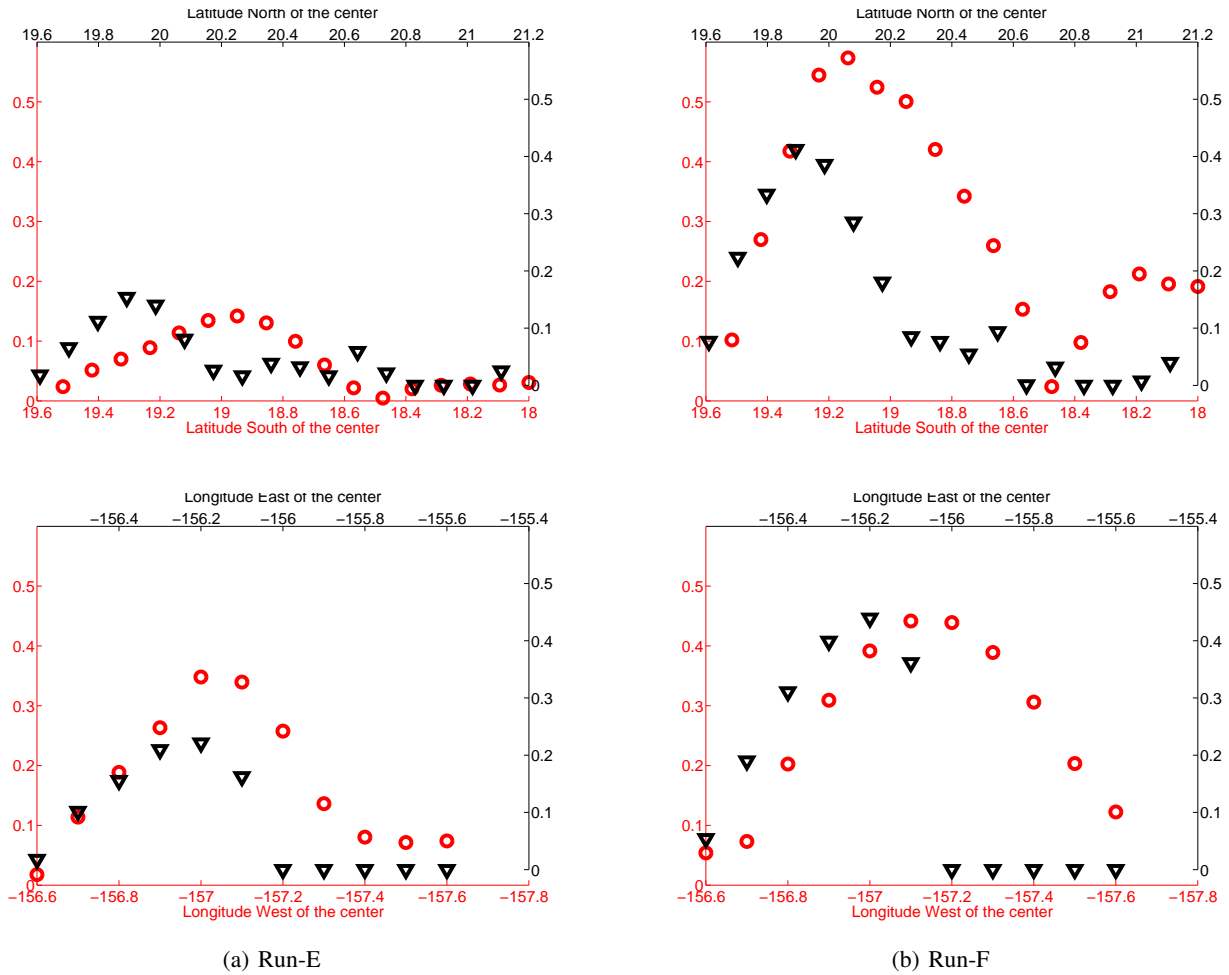
Fig. 13. Distribution of zonal (top) and meridional (bottom) components of the 40-m depth horizontal velocity [m s^{-1}] with respect to the center of the eddy *C5-E* (Run-E, April 13, left) and of the eddy *C1-F* (Run-F, March 28, right).